

GT2010-&&, (

**AERODYNAMIC PERFORMANCE OF A VERY HIGH LIFT LOW PRESSURE
TURBINE AIRFOIL (T106C) AT LOW REYNOLDS AND HIGH MACH NUMBER WITH
EFFECT OF FREE STREAM TURBULENCE INTENSITY**

Jan Michálek

Michelangelo Monaldi

Tony Arts

Turbomachinery and Propulsion Department – “Jacques Chauvin” Laboratory,
von Karman Institute for Fluid Dynamics,
1640 Rhode-Saint-Genèse, Belgium

ABSTRACT

A detailed experimental analysis of the effects of the Reynolds number and free-stream turbulence intensity on the aerodynamic performance of a very high-lift, mid-loaded low-pressure turbine blade (T106C) is presented in this paper. The study was carried out on a large scale linear cascade in the VKI S1/C high-speed wind tunnel, operating at high exit Mach number (0.65) with a range of low Reynolds numbers (80,000 - 160,000) and three levels of free-stream turbulence intensity (0.8 - 3.2 %). In the first part of the paper, the overall aerodynamic performance of the airfoil is presented, based on mid-span measurements performed by means of static pressure taps, hot-film sensors and a 5-hole probe traversing downstream of the cascade. Some specific features of separated flow transition are also discussed for selected cases. The second part presents the analysis of the results in terms of correlations derived for the characteristic points of boundary layer separation and transition. A comparison with some previously published prediction models is shown. The large variety of boundary conditions provides a unique database for validating codes dealing with separated flow transition in turbomachinery.

NOMENCLATURE

c	Chord
E	Hot-film voltage
f	Frequency
FSTI	Free-stream turbulence intensity
g	Pitch
h	Span
K	Acceleration parameter
L _i	Integral length scale

M	Mach number
p	Pressure
Re	Reynolds number
s	Curvilinear coordinate
u,v	Fluctuating parts of velocity components
V	Velocity
<i>Greek symbols</i>	
β	Flow angle
γ	Intermittency
κ	Isentropic exponent
λ	Taylor microscale
η	Kolmogorov scale
ν	Kinematic viscosity
τ	Quasi-wall-shear stress
ζ	Kinematic loss coefficient
<i>Subscripts</i>	
0	Total condition
1	Upstream condition
2	Downstream condition
ax	Axial
o	Reference length
prec	Pressure recovery
R	Reattachment
s	Curvilinear coordinate
S	Separation
t	Transition onset
∞	Free-stream

INTRODUCTION

The pursuit for higher bypass ratios in modern commercial jet engines requires low-pressure (LP) turbines to provide an increasingly larger power output allowing to drive large diameter fans without penalizing the efficiency. At the same time, the actual design trend is oriented toward a reduction of their blade count, in order to save weight and secure lower manufacturing and operating costs. This implies an increase of the aerodynamic load on each blade, leading to the development of very-high-lift airfoils. These are characterized by a higher velocity peak on the suction side, followed by a considerable diffusion. The resulting strong adverse pressure gradient may induce separation of the suction side boundary layer, particularly under low Reynolds number conditions, which causes a significant loss in lift and a consequent drop in engine efficiency (Mayle, [1]). For large commercial turbofans, a loss in LP turbine efficiency of the order of 2 % may occur between sea-level take-off conditions (Volino and Hultgren, [2]), when the Reynolds number in the LP turbine is typically around $5 \cdot 10^5$, and high-altitude cruise flight, when Re is about $5 \cdot 10^4$ (Hodson and Howell, [3]). Curtis et al. [4] showed that the suction side boundary layer is the primary source of losses in the LP turbine, with the eventual separation bubble having the main detrimental effect. Consequently, analyzing and predicting the evolution of the suction side boundary layer is of utmost importance to improve engine design.

Due to the low cruise Reynolds number conditions, a large part of the boundary layer around LP turbine blades may be transitional (Mayle, [1]). Since turbulent flows are much more resistant to separation than laminar ones, the precise prediction of transition development is particularly vital in the case of very-high-lift airfoils, for which the high initial acceleration tends to keep the suction side boundary layer laminar until past the velocity peak even in presence of a significant free-stream turbulence intensity. If the subsequent diffusion is large enough, a laminar boundary layer is not able to withstand the resulting adverse pressure gradient and separates from the blade surface. Volino [5] observed that, in this kind of situation, a laminar boundary layer is likely to separate just after the suction peak. However, if transition occurs soon enough in the separated shear layer, it causes the flow to reattach. Transition and separation are thus affecting each other: understanding the physics behind these processes and learning to predict and possibly control them is crucial for the development of lighter and more efficient jet engines, cheaper to build and to operate.

Mayle [1] classified three modes of transition: natural transition, initiated by Tollmien-Schlichting waves and typical of attached, very low turbulence flows; bypass transition, caused mainly by high free-stream turbulence intensity; separated-flow transition, which takes place in the shear layer over a separation bubble. He considered the last mode to be by far the most important one for LP turbine applications. He also

classified the separation bubbles in two different types, long or short, basing the distinction on the bubble effect on the global pressure distribution along the suction side, rather than on the physical length of the bubble itself. While long bubbles are associated with a greatly modified pressure distribution, high losses and relevant reduction of the exit flow angle, short bubbles have only a local displacement effect and, before and after them, the pressure distribution is close to the one predicted without any separation. Therefore, short bubbles can be an effective way to force the transition of the boundary layer, avoiding losses augment and thus controlling the blade performance. The change in the bubble type, from short to long, is called bursting, which according to Mayle, is an unsteady process which can be triggered even by small changes in either the Reynolds number or the angle of attack. He claimed that the topological difference between short and long bubbles is not the length of the transition, which is independent on the type of bubble, but rather the length of the unstable laminar shear layer. Mayle also provided a prediction model based on the assumption that the separated flow transition ends at the reattachment point, whereas Walker [6] pointed out that the flow may still be transitional at the reattachment and the end of transition may occur well after the pressure recovery process is completed.

Hatman and Wang [7, 8, and 9] confirmed Walker's statement after performing low speed experiments on a flat plate with a low turbulence intensity and a constant adverse pressure gradient. They considered separated-flow transition as the result of the superposition of two types of instability: Tollmien-Schlichting viscous instability and Kelvin-Helmholtz inviscid instability. Then, they described three different types of separation bubbles: short bubbles with transitional separation, short bubbles and long bubbles, both of the laminar separation type. The predominance of one type of instability determines the mode of transition and thus the type of the bubble.

Volino and Hultgren [2] continued on the same path indicated by Hatman and Wang, but considering both low and high free-stream turbulence intensities (0.5 % and 9 %). They observed that the Reynolds number and the free-stream turbulence intensity do not have a significant effect on the separation point, provided the boundary layer does not undergo transition before separation. Under low free-stream turbulence conditions, the boundary layer is laminar at separation and transition occurs in the shear layer following the natural mode. Under the high free-stream turbulence conditions, at low Reynolds numbers, they found that the boundary layer is still laminar at separation and the location of separation is not changing so much. But the separated boundary layer undergoes transition in bypass mode due to the increased turbulence level. At relatively high Reynolds number, the boundary layer transition occurs before separation and the resulting bubble is short, if any. These results thus agreed very well with those obtained by Hatman and Wang.

Volino [10] then pushed the analysis further, applying the same approach to a real cascade of LP turbine blades. Again, he found the model of Hatman and Wang to be reasonable: all the cases investigated fitted the laminar separation long bubble type. On the other hand, he pointed out that a Tollmien-Schlichting instability mechanism drives transition even when the free-stream turbulence intensity is relatively high. He also stated that predicting the exact location of the separation is not easy, due to its interdependence on the local flow acceleration, while a prediction of transition and reattachment is even more difficult. Particularly, he found Hatman and Wang correlations unable to predict transition and reattachment for low turbulence intensity values. He observed that transition onset is marked by the beginning of a rise in the time-averaged turbulent shear stress, pointing out that higher Reynolds number and free-stream turbulence intensity values move the transition upstream.

Houtermans et al. [11] in their investigation, after obtaining results in a good agreement with those described by Hatman and Wang, also gave support to this last observation by Volino.

The first objective of this paper is to investigate the influence of Reynolds number and free-stream turbulence intensity on the aerodynamic performance of a very high-lift mid-loaded LP turbine blade at high-speed conditions. The second aim is to propose correlations derived for some characteristic points of laminar separation transition process and compare them with some generally accepted prediction models established on low speed measurements.

MEASUREMENTS SETUP AND APPARATUS

Experimental Facility. The results of measurements presented in this paper were obtained in the high-speed closed loop cascade facility S-1/C of the von Karman Institute (**Fig. 1**). This facility allows adjusting independently the levels of density and pressure ratio. A wide range of (high) Mach and (low) Reynolds numbers can therefore be matched. The air flow generated by an axial compressor successively passes across a water cooler, then through a diffuser part, serving as a settling chamber with necessary meshes and honeycombs, and via a convergent part and a rectangular duct before it is delivered to the test section.

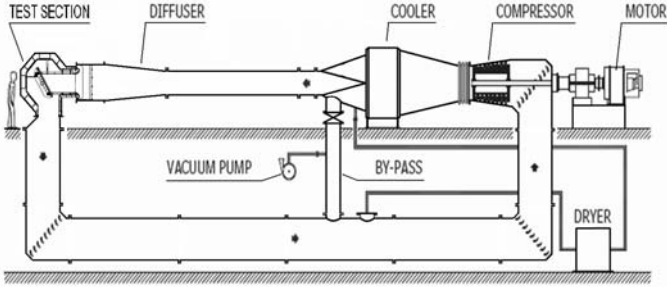


Fig. 1. The S-1/C high speed, variable density wind tunnel

A linear cascade, consisting of six prismatic high-scaled T106C blades, constitutes the test section with a span of 0.225 m and a height of 0.52 m. The T106C is classified as a very high-lift mid-loaded LP turbine airfoil, characterized by a suction side velocity peak at $\sim 0.5 s/s_0$ followed by a strong flow deceleration towards the TE. The main cascade characteristics are listed in **Tab. 1**.

Tab. 1 Main cascade characteristics

Chord c	mm	93.01
Pitch to chord g/c	-	0.95
Aspect ratio h/c	-	2.40
Blade stagger	deg	30.7
Inlet flow angle β_1	deg	32.7
Diffusion factor	-	0.42
Zweiffel coefficient. (incompressible.)	-	1.292

Experimental Apparatus. The experimental arrangement allows placing blades instrumented either with pressure taps or hot-film sensors at the center of the cascade model (the 3rd airfoil from the top). Both types of sensors were positioned at the blade midspan and deployed regularly along the suction side length: 31 pressure taps and 16 hot-film gauges were used respectively. A pressure scanner system was used for the time-averaged pressure measurements.

The hot-film measurements were performed in an alternate order (odd, then even sensors) in two subsequent acquisitions to minimize the thermal interference of neighboring sensors. Moreover, the hot-films sensors could not be calibrated and their output was processed in a semi-quantitative manner (Hodson, [12]). The value of the quasi-wall-shear stress is related to the actual voltage reading and the one for zero-flow conditions (Eq. 1).

$$\tau_w \propto \left(\frac{E^2 - E_0^2}{E_0^2} \right)^3 \quad [1]$$

Time-averaged upstream total pressure was measured by a fixed Pitot probe at 40 % of the inlet duct span. Its span-wise distribution allowed to characterize the inlet end-wall boundary layer. The latter was shown to be turbulent (shape factor ~ 1.4) and its thickness was 15 % of the span for the test regimes applied in the present study.

Pitch-wise distributions of time-averaged flow angles and total pressure were measured upstream and downstream of the cascade by means of a 3-hole and a 5-hole probe respectively. The former was positioned at an axial distance of $0.95 x/c_{ax}$ upstream of the LE and the latter at $0.55 x/c_{ax}$ downstream of the TE. Both probe types were calibrated for a range of Mach numbers (0.3-0.7) and of yaw angles (± 15 deg). The mass-weighted kinetic energy loss coefficient was calculated downstream of the cascade as:

$$\zeta = 1 - \frac{1 - (\overline{P_2}/\overline{P_{02}})^{\kappa-1/\kappa}}{1 - (\overline{P_2}/\overline{P_{01}})^{\kappa-1/\kappa}} \quad [2]$$

Upstream and downstream periodicities were quantified in terms of flow angles, static and total pressure and velocity fields and found to be satisfactory. An X-hot-wire probe (wire length 2 mm, diameter 9 μm) was used to obtain the basic turbulence characteristics of the incoming flow. Similarly to the pneumatic probe measurements, the hot wire pitch-wise traverses were made at axial distance of 0.95 x/c_{ax} upstream of the LE plane.

All pneumatic measurements were sampled at 200 Hz for 10 seconds. The hot-film and hot-wire signals were sampled at 50 kHz and low-pass filtered at 12 kHz, considering the frequency response of both sensors.

Uncertainty. The uncertainty was estimated for all adopted measurement techniques within the full range of the flow conditions. In the following, the values are given for maximum and minimum Reynolds number. Relative uncertainties on the kinetic energy losses were calculated ranging between 10 - 20 %. The absolute flow angle uncertainty varied between 0.2 - 0.3 deg. Relative uncertainties on isentropic Mach number and Reynolds number ranged between 0.4 - 1.2 % and 0.5 - 1.3 %, respectively. The uncertainty on turbulence intensity was estimated to be 12 %. Relatively high values of uncertainty are due to the fact that the measurements were performed at very low pressure (~ 0.1 bar).

Turbulence Grid. A passive turbulence grid was employed upstream of the cascade in order to generate distinct levels of free-stream turbulence intensity. The natural inlet turbulence intensity of the facility is 0.9 %. The grid was designed following suggestions given by [13, 14] resulting in a spanwise parallel array of cylindrical rods of 3 mm in diameter and presenting a mesh size M = 12 mm (the solidity is 0.25). This solidity value satisfies the stability criteria given in the two references above. Increased levels of turbulence intensity were obtained by installing the grid normal to the incoming flow at different stream-wise positions upstream of the cascade. This procedure allowed to define a decay law. A fair agreement with the data presented by Roach [13] was obtained ($Tu = C(x/d)^n$, C = 0.7-0.9, n = -5/7). In this way, the values of turbulence intensity were subsequently calculated at the datum blade LE. For three different grid positions, defined as Grid 1, Grid 3 and Grid 5 (respectively at a distance of 25, 37 and 57 times the mesh size upstream of the LE), the corresponding turbulence intensity values were 3.2, 2.4 and 1.8 percent. These values correspond to the regime at $Re_{2,is} = 120,000$. Although the level of turbulence depends on the geometry and the flow passing through the grid (hence on Reynolds number and pressure drop) the values only varied within ± 0.1 % for

all considered regimes. The turbulence isotropy was finally estimated with and without the grid in a plane normal to the blade span by means of the X-hot-wire probe. In the case of the No Grid configuration the value of about $\overline{u^2}/\overline{v^2} = 0.9$ was estimated (u and v are the fluctuating parts of the velocity components, respectively parallel and normal to the flow). With the grid in the closest position to the LE, the typical values were about 1.2. The latter value could be possibly related to the anisotropic nature of relatively large eddies formed downstream of the grid.

Taylor's frozen turbulence approximation was adopted in order to estimate the characteristic length scales linked to the generated turbulence pattern [15, 16, and 17]. Some of the computed values are listed in **Tab. 2**.

Tab. 2 Computed longitudinal length scales in meters ($Re_{2,is} = 120,000$)

	L_I	λ	η
No Grid	0.004	$7.4 \cdot 10^{-3}$	$0.5 \cdot 10^{-3}$
Grid 1	0.012	$4.4 \cdot 10^{-3}$	$0.3 \cdot 10^{-3}$

While the order of magnitude of Taylor microscale, λ , and Kolmogorov scale, η , were found to be identical with and without the grid, the integral scale L_I showed a larger difference. With the grid in place, $L_I = 0.012$ m corresponds to the grid mesh size or to the order of magnitude of the end-wall boundary layer thickness. The value calculated without the grid was $L_I = 0.5$ m, indicating that, in spite of the fine meshes and honeycombs inside the settling chamber, a large scale pattern seemed to develop through the inlet duct (0.5 m is approx. the channel height). These relatively low frequency periodic events could be possibly related to the convergent part in the settling chamber. However, neglecting this content, the integral length scale was found to be 0.004 m, comparable to the size of the honeycomb cells.

Test Matrix. A wide test matrix consisting of several Reynolds numbers (250,000 - 80,000) based on exit isentropic velocity and chord length and of one fixed isentropic exit Mach number (0.65) was studied. The lowest Reynolds number regime is engine-representative in the last LP turbine stages of modern aircraft engines. The effect of turbulence was investigated in addition, looking at the configurations of Grid 1 (FSTI = 3.2 %) and Grid 5 (FSTI = 1.8 %) for the full range of Reynolds numbers.

RESULTS

Effect of Reynolds Number. **Fig. 2** shows the midspan isentropic Mach number evolution along the suction side of the T106C blade for the No Grid configuration (FSTI = 0.9 %). It is complemented by the numerical prediction provided by a fully turbulent 2D Navier-Stokes computation (Baldwin-Lomax turbulence model, a structured C-type mesh, boundary

conditions corresponding to the highest Reynolds number of the experiments). Details about the code can be found in Arnnone [18].

In all studied cases the Mach number distribution shows a deviation from the fully turbulent prediction, clearly caused by a boundary layer separation. The latter is a consequence of the low Reynolds number and the high adverse pressure gradient existing downstream of the velocity peak. The obtained values of normalized mass-weighted kinetic energy losses and exit flow angle reduction are presented in **Fig. 3** and **Fig. 4**, respectively.

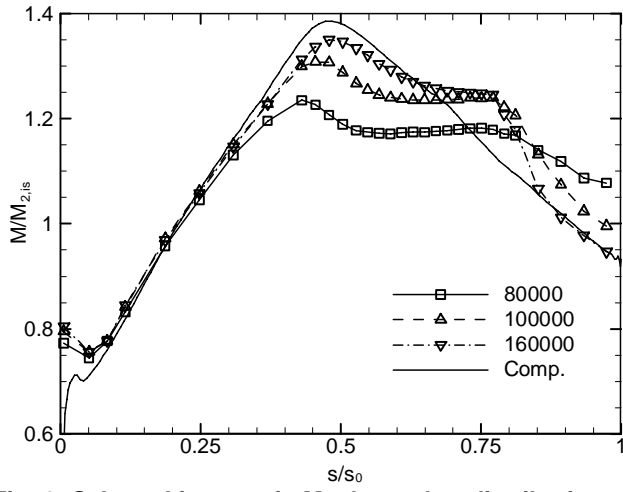


Fig. 2. Selected isentropic Mach number distribution along the suction side of the T106c airfoil for three different $Re_{2,is}$; No Grid

The isentropic Mach number distributions (**Fig. 2**) clearly demonstrate the crucial impact of Reynolds number upon the flow structure. For the highest Reynolds numbers (above 140,000) the flow reattaches to the surface prior to the TE and thus forms a separation bubble with a modest rise of the losses and a limited impact on the velocity distribution. The lowest Reynolds number values ($Re_{2,is} = 80,000 - 100,000$) are on the contrary, liable to an open separation with a perturbed circulation around the blade accompanied by a tremendous loss augmentation (**Fig. 3**) and a significant drop of the turning (**Fig. 4**).

It is worth mentioning that a comparison of the downstream traverses through the wakes (not shown) clearly indicates that the loss increase originates primarily from the airfoil suction side for all the studied flow regimes.

Between the two extreme situations described above, a progressive rise of the losses is put in evidence going towards lower Reynolds numbers. This is linked to the bursting of the separation bubble on the airfoil suction side from the short type to the long one (bursting conditions are indicated in **Tab. 3**). In order to have a better insight to the problem, a deeper investigation of the boundary layer status was performed by means of the hot-film gauges deployed along the blade suction

side. This kind of analysis assumes that the state of the free shear layer within the separated region is, to some extent, transmitted through the bubble to the sensors on the surface [19]. This is supported in the present study by the presence of a grid peak ($f \sim 8900$ Hz) in the frequency spectra of all the sensors, even those in the separated region.

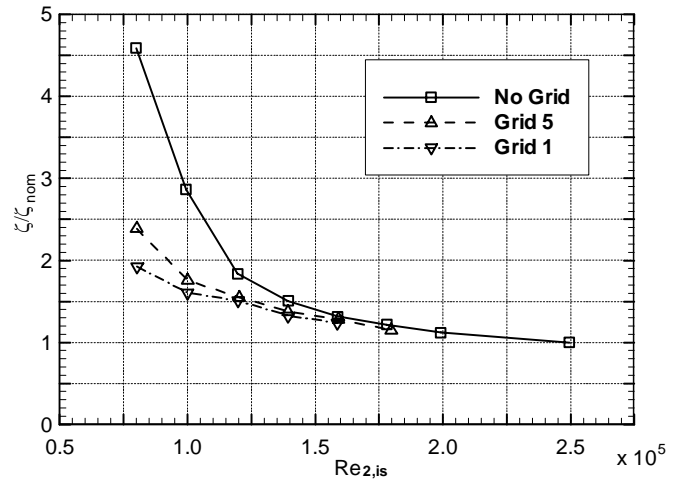


Fig. 3. Mass-weighted kinetic energy losses for three turbulence intensity levels as a function of $Re_{2,is}$

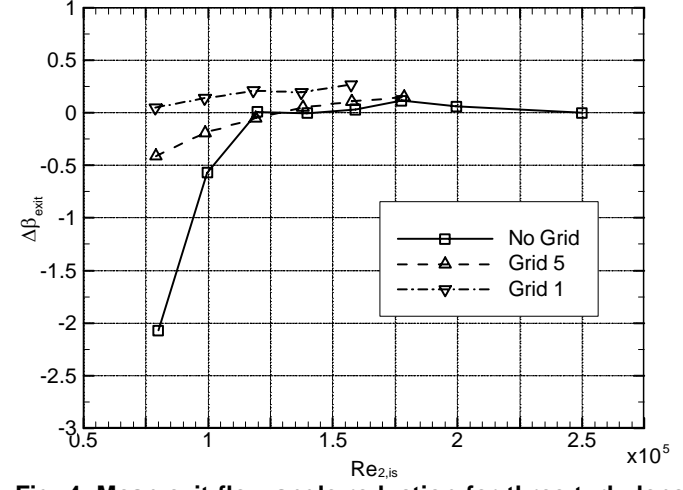


Fig. 4. Mean exit flow angle reduction for three turbulence intensity levels as a function of $Re_{2,is}$

The characterization of the boundary layer status can also be made by using a local intermittency factor based on the power spectrum density integral (PSDI). The intermittency factor used in the present paper (Eq. 3) was originally proposed by Coton et al. [20] and adopted within recent studies in order to provide another indicator describing transition within a boundary layer (besides the classical rms value).

The idea of the intermittency factor is based on the fact that, through the transitional process, the energy of the signal progressively shows a higher frequency content reflected in

higher value of the PSDI. This definition relates the actual value of the PSDI to the one for a laminar (PSDI_L , $\gamma_{\text{PSDI}} = 0$) and for a fully turbulent state (PSDI_T , $\gamma_{\text{PSDI}} = 1$). However, the measurements showed that in the separated region this value can locally exceed unity. This could be possibly attributed to an enhanced production of turbulent energy close to the reattachment point and thus a value above the one of the turbulent flow in the attached boundary layer. Hence this fact locally masks the process in the above detached shear layer. Despite its quantitative estimation, the intermittency factor provides rather a qualitative insight of the problem.

$$\gamma_{\text{PSDI}(s)} = \frac{\text{PSDI}(s) - \text{PSDI}_L}{\text{PSDI}_T - \text{PSDI}_L} \quad [3]$$

The Reynolds number effect is put in evidence by the two cases presented below, $\text{Re}_{2,\text{is}} = 160,000$ and $\text{Re}_{2,\text{is}} = 100,000$ for the No Grid configuration. **Fig. 5** presents a composite picture of the evolution of the quasi-wall shear stress (Eq. 2), its rms value and the intermittency factor obtained for $\text{Re}_{2,\text{is}} = 160,000$. The corresponding frequency spectra and time traces of the signals given by the hot-films are shown in **Fig. 6** for selected points along the blade suction side.

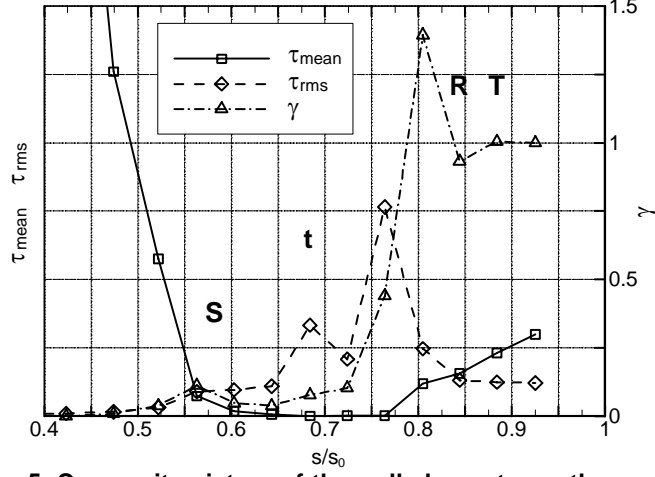


Fig. 5. Composite picture of the wall-shear stress, the rms and the intermittency factor evolution along the suction side at $\text{Re}_{2,\text{is}} = 160,000$ and No Grid (S = separation, R = reattachment, t = onset of transition; T = end of transition)

Upstream of the throat ($s/s_0 = 0.47$), in the accelerating part of the laminar boundary layer, the signals exhibit small fluctuations with a low energy content ($s/s_0 = 0.25$ in **Fig. 6**), besides the spectral peaks related to the large periodic flow structures generated upstream of the cascade (fundamental frequency $f \sim 170$ Hz plus the harmonics). Unfortunately, these perturbations do not seem to damp out while convecting along the blade passage, as the same peaks appear in all the spectra

up to the TE. Downstream of the suction side velocity peak, the time-averaged wall shear stress drops rapidly from its maximum value due to the steep flow deceleration (**Fig. 5**); the rms shows its minimum values and the intermittency factor is also close to zero, indicating that the boundary layer is still laminar.

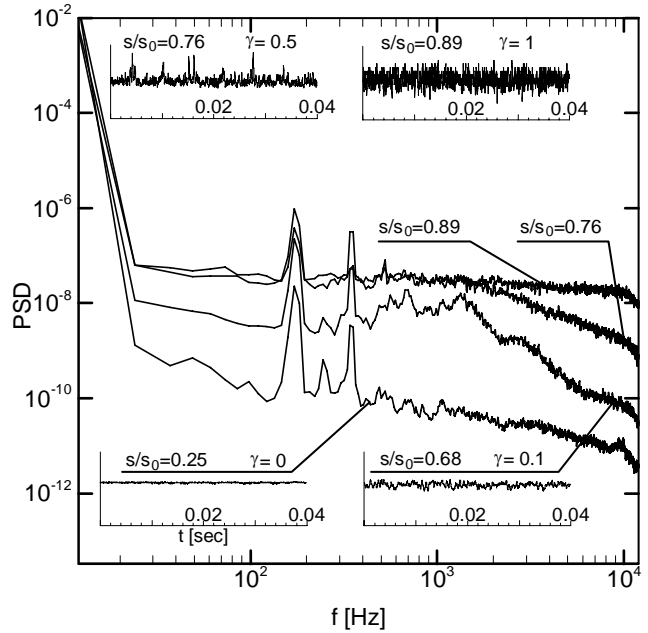


Fig. 6. Composite picture of power spectral density and time traces of hot-films sensors signals at selected points along the suction side; $\text{Re}_{2,\text{is}} = 160,000$, No Grid

At location $s/s_0 = 0.56$, just before the separation, both the rms and the intermittency factor slightly rise. The corresponding power spectrum (not shown) reveals an overall increase of the energy content, which can be associated with the strong deceleration inducing a destabilizing effect on the boundary layer. However, compared to the spectra obtained at $s/s_0 = 0.47$ and $s/s_0 = 0.52$ (not shown), where $\tau_{\text{rms}}, \gamma \sim 0$ and the boundary layer is laminar, the high frequency content does not rise. This implies that the boundary layer is also laminar at this position. The rise in the low frequency range (around 1,000 Hz) was linked to the effect of the bubble on the upstream flow.

The separation is located between $s/s_0 = 0.56$, where $\tau_{\text{mean}} > 0$, and $s/s_0 = 0.60$, where $\tau_{\text{mean}} \sim 0$. The onset of transition takes place at $s/s_0 = 0.68$, where both the rms and the intermittency factor rise from the near-zero values. This can be explained by the periodical ejection of flow from the near-wall region into the shear layer, as described by Hatman and Wang [9]. The corresponding spectrum shows an increase of energy content around 1,000 Hz and 2,500 Hz, but also an elevation in the highest frequency range. The lower frequencies are associated with the unsteady nature of the separation bubble,

while the rise in the higher band is considered as the beginning of the transition.

Further downstream, an abrupt evolution of the transition process takes place. The sensor at $s/s_0 = 0.76$ presents the maximum rms value, which, by definition, indicates the mid-transition point and is related to a region of intensive mixing. The associated power spectrum presents a sudden increase towards a fully turbulent state, while the time trace highlights an undergoing transition process by means of peaks with large positive amplitude embedded in the low amplitude signal. The mid-transition point is found to be coincident with the pressure recovery point present in the velocity distribution (**Fig. 2**).

The reattachment region is located between $s/s_0 = 0.80$, where τ_{mean} rises from zero to a positive value, and $s/s_0 = 0.84$, where the velocity distribution falls back on that computed by the fully turbulent N-S solver. This slight difference between hot-film and pressure data can be explained by the distance along which the velocity profile recovers from the separated-flow type to the fully-attached one. Moreover, it is not possible to determine a single, precise location for the reattachment, due to its unsteady nature connected with the shedding of vortical structures (Hatman and Wang [9]).

Finally, the end of transition occurs at $s/s_0 = 0.89$, since after this point the power spectra do not change anymore, showing an almost constant level of energy throughout the frequency range. The process described up to now is characteristic of the laminar separation short bubble mode. However, there is a discrepancy with respect to the model proposed by Hatman and Wang [8], which specifies that the mid-transition point is located at the reattachment, while the presented study found it to be rather coincident with the pressure recovery point.

A qualitatively different separated flow mechanism was found for the lower Reynolds numbers. **Fig. 7** presents the data provided by the hot-films for $Re_{2,\text{is}} = 100,000$.

The separation of the boundary layer occurs in between the two sensors at $s/s_0 = 0.52$ and 0.56 , which is slightly upstream of the position found for the previous case ($Re_{2,\text{is}} = 160,000$). The peak of the rms, just before the separation, is even more pronounced, indicating a greater streamline deflection caused by a bigger displacement effect of the bubble on the flow. As in the previous case, no characteristic marks of transition onset were detected at this location. The evolution of the wall shear stress in the separated flow region shows two distinctive zones where non-zero values are observed. These suggest a back flow caused by two vortices located inside the separation bubble. The fact that these vortices are seen in the time-averaged signal indicates their quasi-steady nature. It is a characteristic feature of the laminar separation long bubble mode [9, 21]. The onset of transition is found at the same position ($s/s_0 = 0.68$) as for the higher Reynolds number case, one sensor upstream of the maximum rms value ($s/s_0 = 0.72$) which corresponds to the fluid injection into the shear layer

observed by Hatman and Wang [9]. This location presents a zero wall shear stress, thus it can not correspond to the “first reattachment-like” point (R1) reported by Hatman and Wang [8]. R1 was instead located at $s/s_0 = 0.76$ and found to correspond to the pressure recovery point of the velocity distribution (**Fig. 2**), rather than to the mid-transition point.

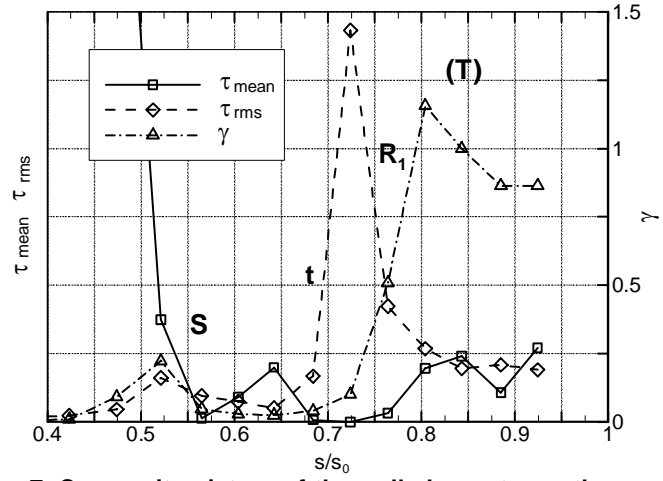


Fig. 7. Composite picture of the wall-shear stress, the rms and the intermittency factor evolution along the suction side at $Re_{2,\text{is}} = 100,000$ and No Grid (S= separation, $R_1 = 1^{\text{st}}$ reattachment, t = onset of transition; T = end of transition)

The end of transition seems to take place at $s/s_0 = 0.84$, where the intermittency shows a value close to unity and the corresponding power spectrum shows a constant level of energy content through the entire frequency band (**Fig. 8**). However, the intermittency drops again downstream of this location. This indicates that turbulence dissipation proceeds at a higher rate than turbulence production, which can be due to the subcritical local Reynolds number and to the weaker vortical structure typical of long bubbles (Hatman and Wang [9]). The power spectrum of the last sensor before the TE ($s/s_0 = 0.93$) is presented in **Fig 8**, highlighting the reduction of the high-frequency energy content which characterizes this reverse transition phenomenon. Consequently, the low turbulence intensity is not sufficient to transport enough momentum from the free-stream to the shear layer and the flow fails to fully reattach before the TE.

Both the low and the high Reynolds number cases show the same qualitative behavior from separation to transition onset, as demonstrated by the comparison of the power spectra in **Fig. 6** and **Fig. 8**. The only difference in this region is the extension of the unstable laminar shear layer, which in the long bubble is slightly longer than in the short one, as also observed by Mayle 1. In fact, while the onset of the transition occurs at the same position ($s/s_0 = 0.68$) for both cases, the boundary layer separates earlier at the lower Reynolds number ($s/s_0 = 0.52-0.56$ instead of $s/s_0 = 0.56-0.60$). However, in the

latter case the onset of transition is positioned closer to the location where the ejection of the fluid into the shear layer takes place ($s/s_0 = 0.72$); this results in the sharp increase of the rms value found in **Fig. 7**. On the contrary, **Fig. 5** shows a broader and less steep rms peak, due to the earlier transition onset caused by the higher Reynolds number.

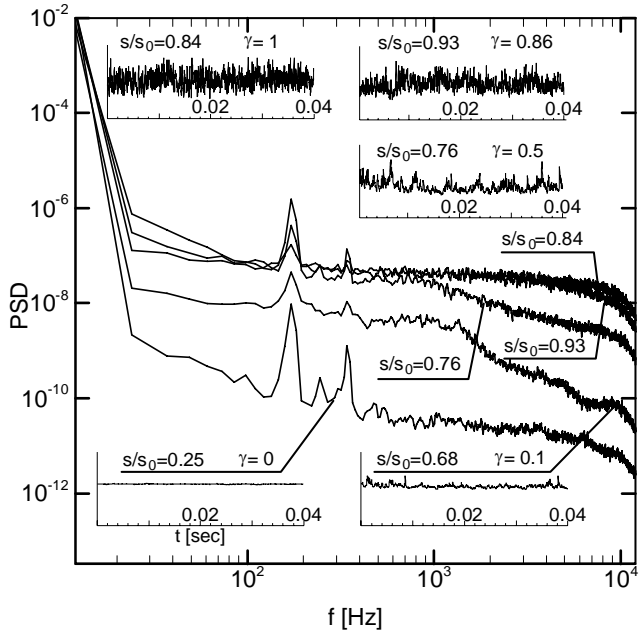


Fig. 8. Composite picture of power spectral density and time traces at selected points along the suction side; $Re_{2,is} = 100,000$, No Grid

However, as also reported by Hatman and Wang [8], the main difference between short and long separation bubbles was found within the transitional part of the shear layer, which shows an extended length for the long bubble type as a consequence of its different topology. The elongated region of the long bubbles is caused by the “re-separation” of the flow (behind point R1) due to the strong adverse pressure gradient and relatively low Reynolds number. The flow reattaches again when the Reynolds number reaches a sufficiently high value in order to complete the transition.

Effect of turbulence intensity. The impact of the different turbulence intensity levels on the Mach number distribution for $Re_{2,is}=100,000$ is presented in **Fig. 9**. The most evident effect of the higher level of turbulence (Grid5, Grid1) is the reattachment of the flow before the TE. As a consequence, the velocity distribution upstream of the separation point remains closer to the one computed by the fully turbulent N-S solver. A further increase of the free-stream turbulence intensity (Grid 1) results in only minor differences observed in the velocity distribution.

This fact is also highlighted looking at the kinetic energy losses in **Fig. 3**. While a moderate rise of the losses occurs when passing from the highest level of turbulence intensity (3.2 %) to the intermediate one (1.8 %), the further drop of the free-stream turbulence intensity (No Grid case) leads to an increase of the losses by a factor of about 1.7. This is mainly related to the transition process at the very end of the blade, as highlighted by the hot-films data shown in **Fig. 10**, corresponding to the results obtained for $Re_{2,is} = 100,000$ and Grid 5 configuration.

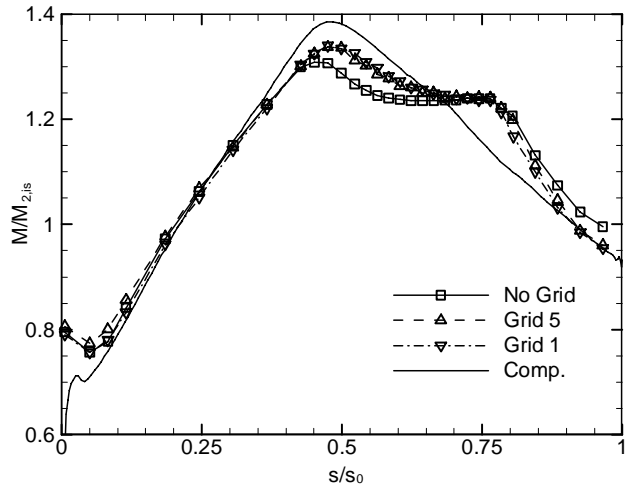


Fig. 9. Isentropic Mach number distribution along the suction side of the T106c airfoil for three different turbulence intensities; $Re_{2,is} = 100,000$

Two main differences were found with respect to the No Grid case at the same Reynolds number: postponed separation ($s/s_0 = 0.60$ instead of $s/s_0 = 0.56$) and the reattachment at the very end of the blade. The former, together with the same position of the transition onset ($s/s_0 = 0.68$), results in a shorter laminar part of detached free shear layer in the case of Grid 5. The latter, as already stated, is the result of the re-energizing effect of the increased free-stream turbulence intensity on the rear part of the separated shear layer. In fact, while both cases show a drop of γ after the end of the transition, for Grid 5 the intermittency then starts to rise again and consequently the flow reattaches before the TE.

The influence of the free-stream turbulence intensity on the flow is larger at low Reynolds numbers. Its effect was observed mainly in the late transition phase, where the free-stream turbulence helps to complete transition even in presence of a subcritical local Reynolds number. It follows that, for higher values of the free-stream turbulence intensity, the Reynolds number effect is reduced. However, it still remains the primary parameter for determining the bubble type and thus the bursting from short to long bubble within the range of the investigated boundary conditions. The situation can change if sufficiently high free-stream turbulence intensity

is considered (not in the present study). Then the transitional separation bubble mode is formed.

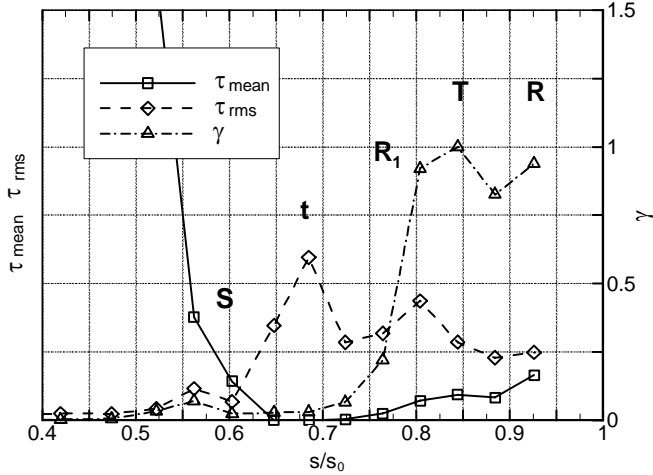


Fig. 10. Composite picture of the wall-shear stress, the rms and the intermittency factor evolution along the suction side at $Re_{2,is} = 100,000$ and Grid 5 (S = separation p., R = -reattachment p., t = -onset of transition; T = end of transition)

Correlations of the characteristic points.

Based on the data analysis presented above, some characteristic points (separation, reattachment, onset of transition, pressure recovery) were determined for all the regimes of the test matrix. As suggested by Hatman and Wang [22], the position of the characteristic points is expressed by a local Reynolds number defined in Eq. 4. These authors reported a better correlation of their data to the local Reynolds number, rather than to a Reynolds number based on displacement or momentum thickness.

$$Re_s = \frac{sV_{\infty,s}}{V_s} \quad [4]$$

In the following, the present results are compared to the prediction model proposed by Hatman and Wang [22]. Their data were obtained for flat plate measurements and limited airfoil data at low turbulence intensity ($FSTI = 0.3 - 0.6\%$).

Separation point. The separation point was defined as the location where the time-averaged wall-shear stress goes to a zero value. However, due to the limited spatial resolution of the hot-film sensors, the velocity distributions were also taken into account. The separation point was thus considered to be just downstream of the location where $dV_{\infty,s}/ds$ shows a local minimum. A good agreement was found with the hot-films data.

The separation location is correlated in terms of the local Reynolds number $Re_{s,S}$ and the acceleration parameter $K_{s,S}$

(Eq. 5) in **Fig. 11**. The results obtained for the No Grid configuration show a fair agreement with those obtained by Hatman and Wang. The data set was fitted by Eq. 6 within the investigated range of acceleration parameters.

$$K_{s,S} = \frac{\nu}{V_{\infty}^2} \frac{dV_{\infty}}{ds} \quad [5]$$

The results for two higher turbulence intensities (Grid 5, Grid 1) denote only minor differences and therefore the data points were all at once fitted by Eq. 7. The effect of raised free-stream turbulence is clearly visible in the lowest range of the acceleration parameter by delaying the separation. As shown in the analysis above, turbulence has mainly an effect within the late transition region (after mid-transition point) of the long bubble type where it causes a shortening of this part and thus alters the conditions at the separation. As such it is considered as indirect. Therefore, for the highest values of the acceleration parameter, and thus the short bubble type, there is a small impact of the increased turbulence on transition since the viscosity effect is predominant. In fact, the data points tend to merge in one line in this region.

The analysis presented in the first part of the paper was performed for all the flow regimes in order to distinguish the type of the separation bubble. Only the laminar separation short and long bubble types were detected within the study (besides the open separation cases). The results are listed in **Tab. 3** with indicated bursting towards lower $Re_{2,is}$ or/and the lower turbulence level.

$$Re_{s,S} \Big|_{NoGrid} = 2540 - 232750(K_s \cdot 10^6) - 65880/(K_s \cdot 10^6)^2 \quad [6]$$

$$Re_{s,S} \Big|_{Grid5,1} = 6860 - 255190(K_s \cdot 10^6) - 94770/(K_s \cdot 10^6)^2 \quad [7]$$

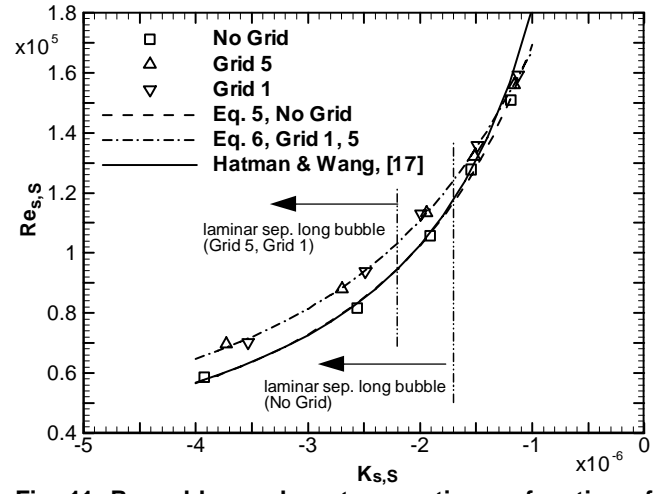


Fig. 11. Reynolds number at separation as function of the acceleration parameter and turbulence intensity

Tab. 3 Identified laminar separation bubble types

(□ short, ○ short/long, △ long, × open), b-bursting

Re _{2,is}	80000	100000	120000	140000	160000
No Grid	×	×	△	b○	□
Grid 5	×	△	b○	□	□
Grid 1	△	△	b○	□	□

The long bubble types for the No Grid configuration were observed in the region delimited as $K_{s,S} < -1.7 \cdot 10^{-6}$ (**Fig. 11**), which indicates a somewhat lower value reported in [22] ($K_{s,S} < -1.3 \cdot 10^{-6}$). This can be due to the high speed compressible boundary layer, real geometry and/or to slightly higher turbulence intensity level. The region for the higher turbulence levels is defined by $K_{s,S} < -2.2 \cdot 10^{-6}$, thus the limit is shifted further towards smaller values of the acceleration parameter (**Fig. 11**).

Pressure recovery point. The position of the pressure recovery point was determined from the velocity distribution as the location where the slope changes rapidly and the diffusion continues. Moreover, as argued by Houtermans et al.[11], the streamlines divergence after the point of maximum bubble height corresponds to a pressure increase and thus can be considered as coinciding with the maximum displacement point. Following this approach, the comparison of the present data with the pressure recovery location provided by Houtermans et al. and the maximum displacement point given by Hatman and Wang is plotted in **Fig. 12**. The proposed correlation between Reynolds number at the separation and the pressure recovery for both types of the separation bubbles in the No Grid case is given by Eq. 7. Similarly, the data points corresponding to the two higher turbulence intensities are linearly fitted by Eq. 8

$$Re_{s,prec}|_{NoGrid} = 32620 + 1.0167 \cdot Re_{s,S} \quad [7]$$

$$Re_{s,prec}|_{Grid5,1} = 29030 + 0.9874 \cdot Re_{s,S} \quad [8]$$

Reattachment point. The reattachment was defined as the location right after the reverse flow region with intensive mixing where the wall shear stress evolution shows a change in slope (sometimes indicated by a local minimum). Similarly as for the point of separation, the blade velocity distributions were used in this case. The correlation of the reattachment to the separation location is presented in **Fig. 13**. Data points lie

in between the models proposed by (Hatman and Wang [22]) and (Houtermans et al. [11])

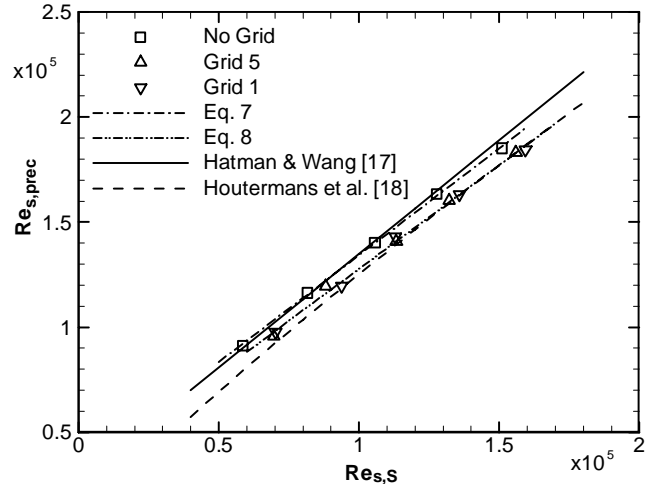


Fig. 12. Reynolds number at the pressure recovery point as a function of Reynolds number at the separation and turbulence intensity,

Despite a lack of points corresponding to long bubbles, the chart indicates the turbulence dependence acting on the length of the separation region. Eq. 9 and 10 represents a linear fitting of the data for Grid 5 and Grid 1, respectively. Data for the No Grid case were not fitted.

$$Re_{s,R}|_{Grid5} = 32435 + 1.0356 \cdot Re_{s,S} \quad [9]$$

$$Re_{s,R}|_{Grid1} = 24733 + 1.0660 \cdot Re_{s,S} \quad [10]$$

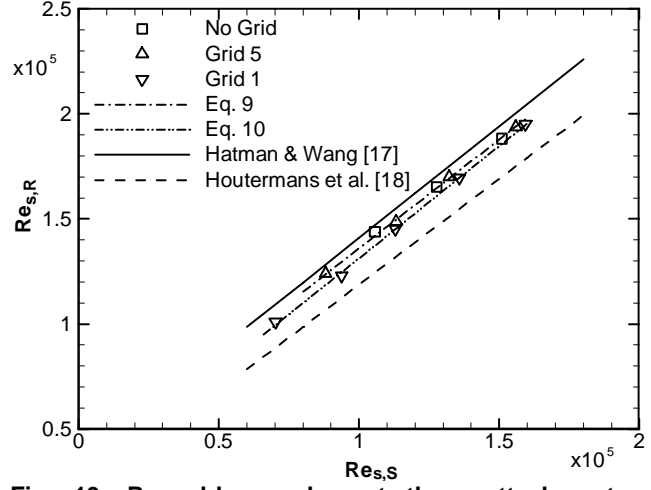


Fig. 13. Reynolds number at the reattachment as a function of Reynolds number at the separation and turbulence intensity,

Transition onset. The Reynolds number at the location of the transition onset is correlated with the Reynolds number at the separation in **Fig. 14**. The data points are sorted according the separation bubble type (rather than turbulence intensity) and a dependency is shown.

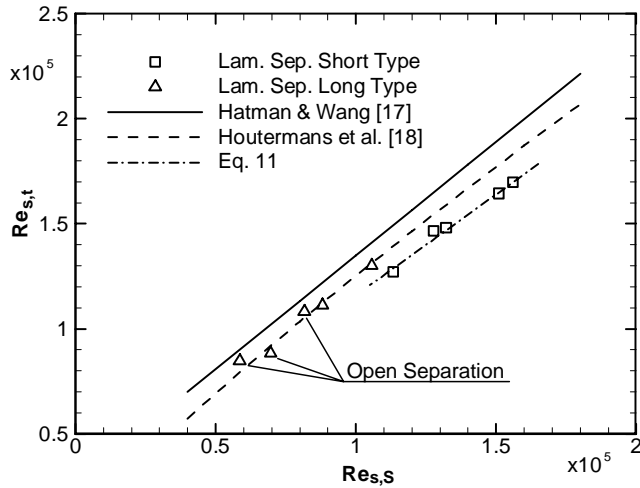


Fig. 14. Reynolds number at the onset of transition as a function of Reynolds number at the separation.

The relative shift can be explained by an extension of the unstable laminar part of the long separation bubble type. The transition onset occurs earlier for both bubble types than the prediction presented by Hatman and Wang [22] and Houtermans et al. [11]. Comparison of the present data in **Fig. 13** and **Fig. 14** points out that for both, short and long bubble types, the onset of transition occurs before pressure recovery. Despite of the small number of the points, data corresponding to the short bubble type were fitted by Eq. 11.

$$\left. \text{Re}_{s,t} \right|_{\text{short}} = 20000 + 0.96 \cdot \text{Re}_{s,s} \quad [11]$$

Transition end. The available data with the end of the transition before the trailing edge did not provide enough points to draw a solid conclusion regarding the location of the transition end. It is generally agreed that transition is completed after reattachment point for the laminar separation short bubble type. In case of the laminar separation long bubble type, the measurements on the wall suggests that process ends within the shear layer before reattachment point as also shown in **Fig. 7** and **Fig. 10**.

CONCLUSIONS

The paper presents the overall aerodynamic performance of the very high lift mid-loaded LP turbine blade (T106C) at high speed conditions under the effect of Reynolds number and free-stream turbulence intensity (FSTI). A strong dependence of the Reynolds number on the separated flow region, and thus on the loss evolution, is pointed out mainly in the case of low

FSTI (0.9 %). The abrupt loss increase is found to be consistent with the change of the laminar separation bubble topology (bursting of the separation bubble). A positive effect of free-stream turbulence intensity is highlighted in terms of losses and exit flow angles for two increased FSTI levels (1.8 and 3.2 %). A shift of the bursting conditions toward a lower Reynolds number is also put in evidence. However, small differences in terms of performance between two higher levels of FSTI are reported. Passing from the lowest Reynolds number range toward higher values, the raised level of FSTI first forces the flow to reattach by energizing the free-shear layer and then, for higher values, it acts on shortening the extension of the separated region in the same manner. With further Reynolds number increase, an acceleration of the transition after its onset forces the long separation bubble to become a short one. Within the range of relatively high Reynolds numbers, the effect is not found to be significant with respect to the different FSTI levels.

The analysis allowed deriving simple correlations for some characteristic points (separation, pressure recovery, onset of transition and reattachment). These were compared with previously published models. A good agreement was found mainly with the prediction of Hatman and Wang for the case of low FSTI. This fact can be useful information in order to apply their model (based on low speed measurements) for high speed conditions. A difference is found, however, in the determination of the onset of transition. The present data show a slightly lower local Reynolds number than the other models for the case of the short bubbles (regardless FSTI), indicating that onset of transition takes place slightly before the pressure recovery.

A dependency of the Reynolds number value at separation on FSTI is reported. The separation location is shown to be progressively delayed towards the lower acceleration parameter. A considerably lower value of the acceleration parameter delimiting the regions of the short and long bubbles is also pointed out ($K_{s,s} \sim -2.2 \cdot 10^{-6}$). On the contrary, the pressure recovery and reattachment Reynolds numbers exhibit lower values than those at low turbulence intensity, which leads to a shorter separated flow region.

Finally, it has to be stated that the present analysis does not cover a wide range of the acceleration parameter. However, it points out some differences arising from the fact that the investigation was performed under realistic conditions of LP turbines in terms of Mach number, low Reynolds number, free-stream turbulence intensity and blade geometry.

ACKNOWLEDGMENTS

The reported work was performed within the European research project "Turbulence and Transition Modelling for Special Turbomachinery Applications" (TATMo, 6FP, AST5-

CT-2006-030939). The permission for publication is gratefully acknowledged by the authors.

REFERENCES

- [1] Mayle R. E., 1991, "The Role of Laminar-Turbulent Transition in Gas Turbine Engines", ASME J. of Turbomachinery, **113**, pp. 509-537.
- [2] Volino R. J., Hultgren L. S., 2001, "Measurements in Separated and Transitional Boundary Layers Under Low-Pressure Turbine Airfoil Conditions", ASME J. of Turbomachinery, **123**, pp. 189-197.
- [3] Hodson H. P., Howell R. J., 2005, "The role of transition in high-lift low-pressure turbines for aeroengines", Progress in Aerospace Sciences 41 (2005), pp. 419-454.
- [4] Curtis E. M., Hodson H. P., Banieghbal M. R., Denton J. D., Howell R. J., Harvey N. W., 1997, "Development of Blade Profiles for Low-Pressure Turbine Applications", ASME J. of Turbomachinery, **119**, pp. 531-538.
- [5] Volino R. J., 2002, "Separated Flow Transition under Simulated Low-Pressure Turbine Airfoil Conditions: Part 1-Mean Flow and Turbulence Statistics", ASME J. of Turbomachinery, **124**, pp. 645-655.
- [6] Walker G. J., 1993, "The Role of Laminar-Turbulent Transition in Gas Turbine Engines: A Discussion", ASME J. Turbomach., **115**, pp. 207-217.
- [7] Hatman, A., Wang, T., 1998, "Separated Flow Transition. Part 1-Experimental Methodology and Mode Classification", ASME Paper 98-GT-461
- [8] Hatman, A., Wang, T., 1998, "Separated Flow Transition. Part 2-Experimental Results", ASME Paper 98-GT-462
- [9] Hatman, A., Wang, T., 1998, "Separated Flow Transition. Part 3-Primary Modes and Vortex Dynamics", ASME Paper 98-GT-463
- [10] Volino R. J., 2002, "Separated Flow Transition Under Simulated Low-Pressure Turbine Airfoil Conditions: Part 2-Turbulence Spectra", ASME J. Turbomach., **124**, pp. 656-664
- [11] Houtermans, R., Coton, T., Arts, T., 2004, "Aerodynamic Performance of a Very High-Lift Low Pressure Turbine Blade with Emphasis on Separation Prediction", J. of Turbomachinery, **126**, pp 406-413.
- [12] Hodson H. P., 1984, "Boundary Layer and Loss Measurements on the Rotor of an Axial-Flow Turbine", J. Eng. Gas Turbines Power, **106** (2), pp. 391-399
- [13] Roach, P. E., 1986, "The generation of nearly isotropic turbulence by means of grids", Int. J. Heat Fluid Flow, **7**(2)
- [14] Batchelor, G. K., 1967, "The theory of homogenous turbulence", Cambridge University Press
- [15] Hinze, J. O., 1959, "Turbulence", McGraw-Hill, 1st edn.
- [16] Brunn, H. H., 1995, "Hot-Wire Anemometry, Principles and Signal Analysis", Oxford University Press Inc, New York.
- [17] Bradshaw, P., 1971, "An introduction to turbulence and its measurement", Pergamon Press
- [18] Arnone A., 1994, "Viscous Analysis of a three-dimensional rotor flow using a multigrid method", ASME J. of Turbomachinery, **116**, pp. 435-445
- [19] Zhang, X. F., Mahallati, A., Sjolander S.A., "Hot-Film Measurements of Boundary Layer Transition, Separation and Reattachment on a Low-Pressure Turbine Airfoil at Low Reynolds Numbers", AIAA Paper, 2002-3643
- [20] Coton, T., Arts, T., Lefebvre, M., Liamis, N., 2003, "Unsteady and Calming effects Investigation on a Very High-Lift LP Turbine Blade-Part I: Experimental Analysis", ASME J. of Turbomachinery, **125**, pp. 281-289
- [21] Pauley, L., Moin, P., Reynolds, W., 1990, "The Structure of Two-Dimensional Separation", J. of Fluid Mechanics, **220**, pp. 397-411
- [22] Hatman, A., Wang, T., 1999, "A Prediction Model for Separated Flow Transition", J. of Turbomachinery, **121**, pp 594-602